TRENDS IN SCIENCES 2026; 23(6): 12339
https://doi.org/10.48048/tis.2026.12339 RESEARCH ARTICLE

Rational Design of Micromesoporosity ZSM-5 Incorporated with NiO for the Deoxygenation of *Reutealis trisperma* Oil

Dina Kartika Maharani[1], Riki Subagyo[2], Stella Jovita[2], Khawiyatur Rivah Agustina[2], Hasliza Bahruji[3], Reva Edra Nugraha[4], Nurul Asikin Mijan[5], Aishah Abdul Jalil[6,7], Didik Prasetyoko[2] and Yuly Kusumawati[2,*]

[1]*Department of Chemistry, Faculty of Mathematics and Natural Science, Universitas Negeri Surabaya, East Java 60211, Indonesia*
[2]*Department of Chemistry, Faculty of Science and Data Analytics, Institut Teknologi Sepuluh Nopember, East Java 60111, Indonesia*
[3]*Centre for Advanced Material and Energy Sciences, Universiti Brunei Darussalam, Bandar Seri Begawan BE1410, Brunei Darussalam*
[4]*Department of Chemical Engineering, Faculty of Engineering, Universitas Pembangunan Nasional "Veteran" Jawa Timur, East Java 60294, Indonesia*
[5]*Department of Chemical Sciences, Faculty of Science and Technology, Universiti Kebangsaan Malaysia, Selangor 43600, Malaysia*
[6]*Department of Chemical Engineering, Faculty of Chemical and Energy Engineering, Universiti Teknologi Malaysia, Johor 81310, Malaysia*
[7]*Centre of Hydrogen Energy, Institute of Future Energy, Universiti Teknologi Malaysia, Johor 81310, Malaysia*

([*]Corresponding author's e-mail: y_kusumawati@chem.its.ac.id)

Received: 18 October 2025, Revised: 5 November 2025, Accepted: 15 November 2025, Published: 30 January 2026

Abstract

The porosity and acidic properties of ZSM-5 are crucial factors for its ability to catalyze reactions with large molecules, such as *Reutealis trisperma* oil (RTO). In this work, the textural properties of ZSM-5 were rationally designed by controlling the crystallisation time during synthesis, while the acid content of ZSM-5 was increased by incorporating nickel (Ni) species on the surface of ZSM-5. All the samples exhibited microporous and mesoporous features with many Lewis acid sites. These properties increase the catalytic activity of the conversion of RTO into biofuel. The high composition of micromesoporous and Lewis acid sites in NiZ1 and NiZ1.5 promoted the generation of heavy oil. NiZ3, which has moderate micromesoporous and Lewis acid sites, facilitates the production of diesel hydrocarbons. The low micromesoporous feature and few acid sites in NiZ9 make gasoline hydrocarbons production more feasible. This finding provided the regulation of acid site number and micromesoporous features to facilitate the conversion of RTO into green diesel.

Keywords: Biofuel, Deoxygenation, Ni-ZSM-5 catalysts, *Reutealis triseperma* oil

Introduction

The increasing demand for renewable diesel for vehicles and jet engines has shifted the production from edible resources such as starch and sugar to nonedible sources as part of achieving food and energy security [1]. Triglycerides from nonedible oil can be transformed into C10 - C16 alkane hydrocarbons comprising linear, cyclic or branched structures for jet fuel application [1,2]. A technology for producing hydrocarbon fuel is the gasification of oil, followed by Fischer-Tropsch (FT) synthesis [3-5]. Nonetheless, the primary drawbacks of

this method include higher costs and harmful carbon dioxide emissions. Alternatively, the hydrodeoxygenation (HDO) of plant oils guarantees the formation of long-chain linear hydrocarbon compounds that contain less oxygen, sulfur and aromatics through the HDO reaction [6]. Oxygen from triglycerides is eliminated, followed by oligomerisation to produce unsaturated linear hydrocarbon compounds [7]. The hydrocarbon composition is highly dependent on the nature of the catalyst, which can control the route to HDO, decarboxylation and decarbonylation. Metal sulfides, such as MoS_2 [8,9], CoMoS [10], NiMoS [6], are effective catalysts for deoxygenation (DO) reactions. However, sulfide-based catalysts produce biojet fuel contaminated with sulfur. Additionally, the addition of sulfur sources such as dimethyl sulfoxide and hydrogen disulfide is required to maintain the sulfite state [11]. Precious metal catalysts such as Pd/C [12], Pt/SAPO-31 [13], Pd/Al_2O_3 [14], and Ru/TiO_2 [15,16] have high catalytic activity but suffer from particle sintering at high temperatures [6].

As an alternative, zeolite socony mobile-5 (ZSM-5) has been desired as catalyst for DO reaction because ZSM-5 possesses high thermal stability properties, a selective shape, adsorption ability and acidity [17-19]. The moderate Lewis and Brønsted acidities and textural features reduce steric hindrance and increase thermal stability [20]. Three-dimensional pores with sizes of approximately 5.1 - 5.5 Å are suitable for the formation of hydrocarbons [21,22]. Despite its advantages, researchers have modified ZSM-5 with a combination of microporous and mesoporous features to improve conversion [23,24]. The generation of micropores and mesopores in ZSM-5 typically be accomplished via dealumination or desilication using acidic or alkaline solvents, respectively [25,26]. However, this strategy disrupts the framework of ZSM-5. In another approach, the formation of microporous and mesoporous features can be achieved by controlling the crystallisation time [27,28], which is more advantageous and more controllable. Controlling the crystallisation time can affect the textural features of ZSM-5. For example, Tehubijuluw *et al.* [28] reported the formation of micro-mesoporous features in ZSM-5 by controlling the crystallisation time. This approach results in a high surface area up to 734 m^2/g with micropores (1.18 nm) and mesopores (3.02 nm). Li *et al.* [29] synthesised ZSM-5 by varying the crystallisation time via hydrothermal methods. The longer hydrothermal process at low temperatures resulted in a low surface area with few mesoporous features, whereas the faster hydrothermal process at low temperatures slightly increased the surface area and mesoporous properties. The highly mesoporous features promoted the initial cracking of triisopropylbenzene into diisopropylbenzene, which was subsequently converted into benzene via a deeper cracking process. Wang *et al.* [30] also prepared mesoporous ZSM-5 by decreasing the temperature and duration of the hydrothermal process and then incorporating Pd metal. This strategy improved the surface area and increased the pore diameter. Consequently, the conversion of guaiacol using Pd/Meso-ZSM-5 was 4 times greater than that with Pd/ZSM-5. Notably, the possession of mesoporous features facilitates the diffusion of oil molecules on the surface of ZSM-5 and subsequently converts the molecules into targeted compounds. Nonetheless, the selectivity of ZSM-5 in the DO reaction for diesel hydrocarbons is moderate because of the moderate number of acid sites.

Compared with the cracking reaction, the modification of mesoporous ZSM-5 with transition metals increased the selectivity of the HDO reaction, increasing the paraffin hydrocarbon composition [31]. Ni-based catalysts have been reported to improve the catalytic activity of the DO reaction. Higher conversions (up to 90%) can be achieved with Ni-based catalysts in hydrogen-rich or hydrogen-free environments [32] since Ni catalysts have economic advantages and can proficiently break C–C, C–O and C–H bonds [33]. Ni-based catalysts are thus expected to be appropriate for various reactants to generate green diesel, including triglycerides, cooking oil, and palm fatty acid distillate (PFAD), since the nature of the reactant has little effect on the activity of Ni-based catalysts [32]. In addition to having a high conversion rate, the catalysts yielded product distribution comprising diesel-range alkane hydrocarbons. Earlier, Wang *et al.* [30] reported Ni/Mo supported on ZSM-5 for catalytic hydrocracking of soybean oil [34]. A low reaction temperature (360 °C) resulted in a significant change in selectivity toward hydrocarbon fuels. Botas *et al.* [35] also reported a higher selectivity toward the formation of light olefins using Ni/HZSM-5 during deoxygenation of the rapeseed oil. Li *et al*. [36] reported that the Ni/ZSM-5 catalyst had

high catalytic activity in the HDO guaiacol reaction, with a conversion of 74.8% and high selectivity into cyclohexane of up to 90%. Li *et al.* [36] encapsulated Ni nanoparticles in ZSM-5 for the selective hydrodeoxygenation of phenolics [37]. The presence of Ni improved the number of acid sites. The high number of acid sites provided strong phenol adsorption on the ZSM-5 surface, which was converted into cyclohexane. The presence of Ni on ZSM-5 not only increased the acidity of ZSM-5 but also improved the interaction between molecules and the catalyst, which more easily into targeted compounds and generated high conversion and selectivity.

In this work, we report the rational design of the micromesoporous features of ZSM-5 from kaolin via crystallisation control, which is subsequently deposited with nickel oxide (NiO) via the wet impregnation method. This method yielded the formation of microporous and mesoporous features even after the impregnation of NiO on the ZSM-5 surface. The presence of NiO improved the number of acid sites on ZSM-5. The integration of micromesoporous features and an increased number of acid sites improved the selectivity of green diesel. This finding provides further understanding of the roles of Lewis/Brønsted acid sites and the mesoporosity of Ni/ZSM-5 in the conversion and distribution of hydrocarbons produced from the deoxygenation reaction.

Materials and methods

Materials

Kaolin $Al_4(Si_4O_{10})(OH)_8$ as silica and alumina source was obtained from Bangka Belitung, Indonesia (2°14′ S, 106°10′ E). Kaolin comprises of 57% SiO_2 and 22% Al_2O_3. RTO as feedstock was acquired from Surabaya Indonesia. Both raw materials were used as received without further purification. NaOH (> 99%) was purchased from Merck, Germany. LUDOX®HS-40 colloidal silica (30% Si in water) and nickel(II) nitrate hexahydrate (99%) was purchased from Sigma Aldrich, Germany. N-Cetyl-N,N,N-trimethylammonium bromide (CTABr, $C_{19}H_{42}BrN$, 99%) were purchased from Applichem. All the materials used in this work were of analytical grade. The preparation of materials and DO reactions were performed at the Materials and Energy Laboratory, Chemistry Department, Institut Teknologi Sepuluh Nopember, Indonesia.

Synthesis of the ZSM-5 support

ZSM-5 was prepared from 10 Na_2O: 100 SiO_2: 2 Al_2O_3: 1,800 H_2O in terms of molar composition. NaOH (1.60 g) was dissolved in demineralized water with continuous stirring for 30 min. Kaolin (1.85 g) was added gradually, followed by the addition of LUDOX (37.09 g) under vigorous stirring. Demineralized water was added to the mixture and stirred for 8 h. The resulting gel was aged for 6 h at 70 °C, transferred into an autoclave with a Teflon liner of 330 mL capacity, and heated at 80 °C with crystallization times of 1, 1.5, 3, or 9 h. The autoclave was cooled immediately to stop the crystallisation process. CTABr (18.93 g) as a mesopore template (SiO_2/CTABr ratio = 1/4) was added slowly into the mixture and stirred for 1 h. The crystallisation was continued for another 24 h at 150 °C. The solid product was altered and washed with distilled water until the pH of the supernatant was neutral. The product was oven-dried at 60 °C for 24 h, calcined at 550 °C (2 °C/min) under N_2 for 1 h, and then replaced with air for an additional 6 h.

Synthesis of Ni/ZSM-5

Ni/ZSM-5 catalysts were prepared via the impregnation method. The Ni content was set as 10 wt.%. The calculated amount of $Ni(NO_3)_2{\cdot}6H_2O$ was dissolved in demineralised water (10 mL) under continuous stirring. One gram of ZSM-5 powder was added to the solution and stirred at ambient temperature. The mixture was gradually heated to ~120 °C with regular stirring until the light green suspension became a paste. The product was left overnight at 80 °C. Finally, the resulting dried samples were ground and calcined at 550 °C (2 °C min^{-1}) under N_2 flow for 1 h followed by air flow for 6 h.

Characterization

All the catalysts were characterised using a PHILIPS-binary XPert with an MPD Cu Kα diffractometer for wide-angle analysis. The analysis was performed at a current of 30 mA and 40 kV and scanned from 5° to 80° with increasing steps of 0.020°/s. Low-angle XRD was applied with a Bruker type D2 phaser with KFL Cu Kα radiation at 10 mA and 30 kV. A Fourier transform infrared (FTIR, SHIMADZU 8400S) spectrometer was used to determine the functional groups of the catalysts via the KBr method. For pyridine

FTIR analysis, the samples were calcined at 400 °C for 4 h under N_2 flow. The temperature was subsequently set at 150 °C. After the temperature reached 150 °C, approximately 200 µL of the pyridine solution was dropped, and the mixture was maintained at that temperature for 3 h, followed by cooling to 50 °C. The prepared samples were then analyzed at wavenumbers ranging from 4,000 - 400 cm^{-1}. The surface morphology and elemental distribution of the catalysts were investigated by scanning electron microscopy (SEM, JEOL 6360 LA) and transmission electron microscopy (TEM, Hitachi HR-9500 TEM with an acceleration voltage of 300 kV). The textural properties were determined using N_2 adsorption-desorption on a Quantachrome Touchwin v1.11 instrument. A Quantachrome ASiQwin instrument was used to calculate the pore size distribution via the NLDFT method. Quantachrome ChemBET Pulsar TPR/TPD equipped with a thermal conductivity detector (TCD) was employed to observe the reducibility of samples. X-ray photoelectron spectroscopy (XPS) was used to evaluate the oxidation state of NiZ3 using Kratos Axis Supra XPS.

Catalytic deoxygenation reaction of RTO

The catalytic DO reaction of RTO was performed using a semibatch reactor. Before use, each tool was washed with acetone and n-hexane and dried in an oven. Ten g of RTO and 0.3 g of catalyst were put into a 3-neck round-bottom flask and subsequently set in the reactor. Prior to the reaction, a gas mixture of 10% H_2 and 90% N_2 was flowed into the reactor for 15 min to remove the residual air in the reactor. The mixture was stirred and heated to 350 °C. After the temperature of reactor reached 350 °C, the temperature was held for 4 h to allow the DO reaction to occur. The resulting gas condenses in the condenser with a cooling system from an ice bath for conversion into the liquid phase. The liquid product was collected in an a-neck round bottom flask during the reaction. The collected liquid product was transferred into a sealed bottle and stored in a chiller before GC analysis. The DO reaction was performed twice to ensure that the resulting product was obtained.

Results and discussion

XRD study

The X-ray diffraction pattern of NiZ is shown in **Figure 1**. The rapid crystallisation reaction of 1 and 1.5 h led to the generation of amorphous mesoporous aluminosilicate, whereas the crystallisation time of 3 - 9 h yielded the typical diffraction profile of hierarchical ZSM-5. The typical peaks of hierarchical ZSM-5 arise at 2θ = 7.8, 8.7, 23, 23.8 and 24.0° and are attributed to the 101, 020, 501, 303, and 133 planes, respectively, according to JCPDS No. 44–0003 [38,39]. The deposition of Ni on ZSM-5 via impregnation generates the typical peak of NiO, which appears at 2θ = 37.13° (111) and 43.2° (200) and is attributed to a face-centred cubic structure of NiO (JCPDS 01-075-0197) [40]. This result indicates that NiO particles formed in ZSM-5. The peak intensity of NiO is greater when it is impregnated on ZSM-5 synthesised at longer crystallisation time. Compared with our previous work [41], the typical peak of ZSM-5 is retained even after the impregnation of NiO, revealing the stability of the ZSM-5 framework. The intensity of NiO is also improved when it is impregnated on ZSM-5 for various crystallization times, implying that the crystal size of NiO on ZSM-5 with a fast crystallisation time is smaller than that of NiO impregnated on ZSM-5 with a low crystallisation time. A smaller NiO crystal size indicates better dispersion of NiO on the support materials [42]. The NiO size calculated by Scherrer formula are 31.59, 36.48, 36.48 and 51.07 nm for NiZ1, NiZ1.5, NiZ3, and NiZ9, respectively. The amorphous structure of NiZ1 and NiZ1.5 provides a high amount of Si–OH, which is converted into Si–O–Ni via ion exchange during impregnation and yields a good dispersion of NiO on the surface of the support. When the crystallisation time during ZSM-5 synthesis is increased, the framework of ZSM-5 is more configurable, which decreases the Si–OH number and decreases the ion exchange reaction. Consequently, the generation of NiO crystallites is more feasible, yielding a high XRD intensity of NiO. Overall, the relative crystallinity of the ZSM-5 support on the NiZ3 and NiZ9 catalysts is lower than the crystallinity of the Z3 and Z9 catalysts which show that the deposition of Ni metal on the ZSM-5 support reduces the crystallinity of ZSM-5 [43].

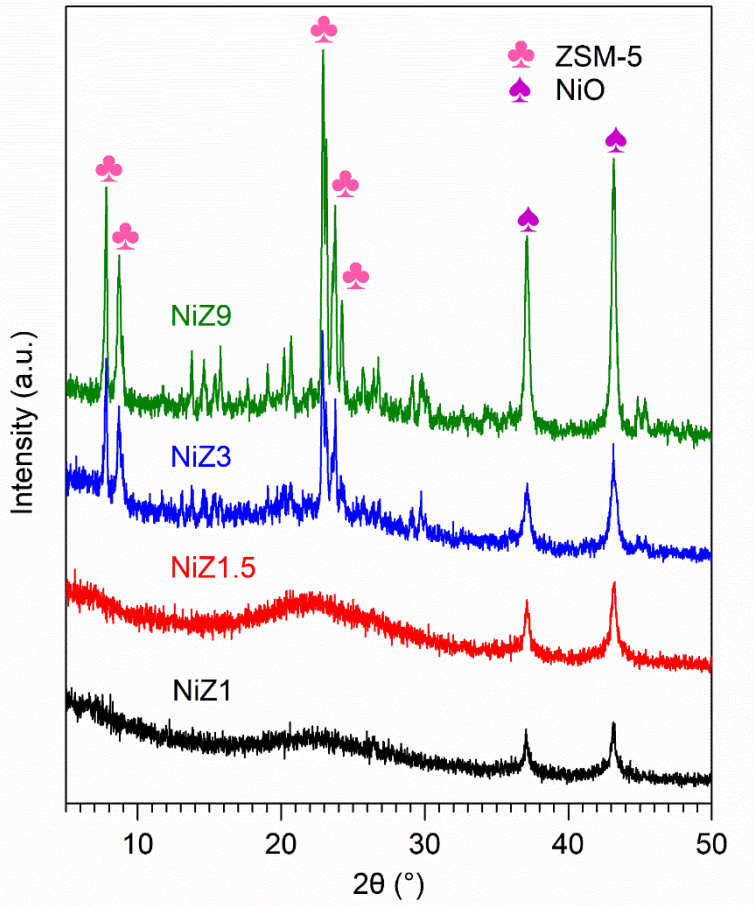

Figure 1 XRD pattern of NiZ samples, including NiZ1 (black line), NiZ1.5 (red line), NiZ3 (blue line), and NiZ9 (green line). All samples were measured at room temperature.

FTIR study

The FTIR spectra of all the catalysts are shown in **Figure 2**. The O–H stretching vibration is typically observed at 3,457 cm^{-1} and is accompanied by the O–H bending vibration at 1,631 cm^{-1} [44]. Consistent with the XRD results, the characteristic vibration of the hierarchical ZSM-5 also arises after the incorporation of NiO. The typical absorption bands of hierarchical ZSM-5 are observed at 441, 548, 785, 1,078, and 1,224 cm^{-1}. The absorption bands at 1,224 and 785 cm^{-1} are attributed to the externally symmetrical vibrations and externally symmetrical vibrations of Si–O–T in ZSM-5 [28]. The absorption band at 1,078 cm^{-1} corresponds to the occurrence of the internal asymmetric stretching vibration of the Si–O–T unit. The absorption peak at 441 cm^{-1} is related to the symmetrical bending vibration of the T–O–T and the O–T–O unit in SiO_4 and AlO_4, whereas the absorption peak at 548 cm^{-1} is associated with the vibration absorption of the five-membered ring (D5R) in the ZSM-5 zeolite framework, which is the characteristic peak of the zeolite of the MFI type [45]. The peak at 1,078 and 1,224 cm^{-1} are sharper with increasing crystallisation time, indicating that the ZSM-5 framework is more configurable. For the NiZ1 and NiZ1.5 catalysts, the absorption peak at 1,100 cm^{-1} was wider and shifted towards a lower wavenumber compared to the NiZ3 and NiZ9 catalysts, which indicated the influence of NiO interactions in the ZSM-5 pore framework structure.

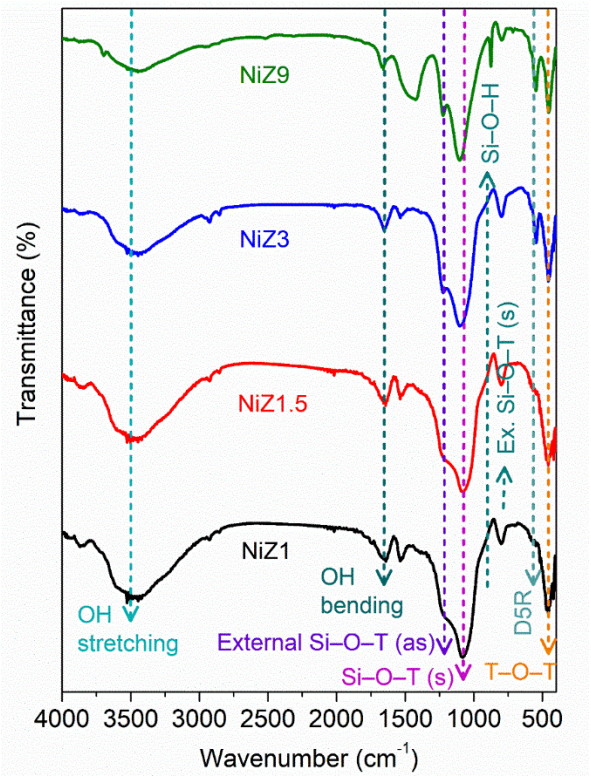

Figure 2 FTIR spectra of NiZ1, NiZ1.5, NiZ3, and NiZ9. The samples were measured at wavenumber of 4,000 - 400 cm^{-1}.

Acidity analysis

FTIR-pyridine spectroscopy was applied to determine the number of acid sites on the NiZ catalyst. Pyridine is used as a probe molecule to determine sample acidity on the basis of the chemical interactions that occur between pyridine and Lewis and Brønsted acid sites. The pyridine FTIR spectrum of NiZ acid catalyst at 150 ℃ desorption temperature is shown in **Figure 3**. The absorption band in the wavenumber region of 1,450 cm^{-1} can be assigned to the Lewis pyridine bond, which is an interaction between the nitrogen atom in pyridine and the Lewis acid sites on the catalyst [46]. The lone pair of pyridine nitrogen is bound by a coordination bond with the empty orbital of the metal from the aluminosilicate structure, resulting in the characteristic absorption of a Lewis acid. The absorption band at 1,545 cm^{-1} is absorption from pyridinium ions with Brønsted acid sites [37], whereas the absorption band at 1,490 cm^{-1} is a combination of pyridine acid interactions with Brønsted and Lewis acids. In addition, the absorption peak intensity of the Brønsted acid sites is considerably lower than that of the Lewis acid sites on all catalysts. The addition of Ni metal increased the number of Lewis acid sites on all the NiZ1, NiZ1.5, NiZ3, and NiZ9 catalysts. Compared with ZSM-5 in our previous work [41], the Lewis acid sites increased on the NiZ catalyst compared with the ZSM-5 catalyst. The presence of Ni reduced the number of protons because of the formation of Ni–O species in the Si–O–Al framework in ZSM-5 [37], and thus, the Lewis acid was improved. As shown in **Table 1**, the crystallisation time affects the number of Brønsted and Lewis acid sites in the NiZ samples. An increase in the crystallization time also increased the number of Brønsted and Lewis acid sites. The increase in Brønsted and Lewis acids indicates saturation in the ion exchange process, which is better for catalysts with mesoporous support structures than for those with microporous support structures.

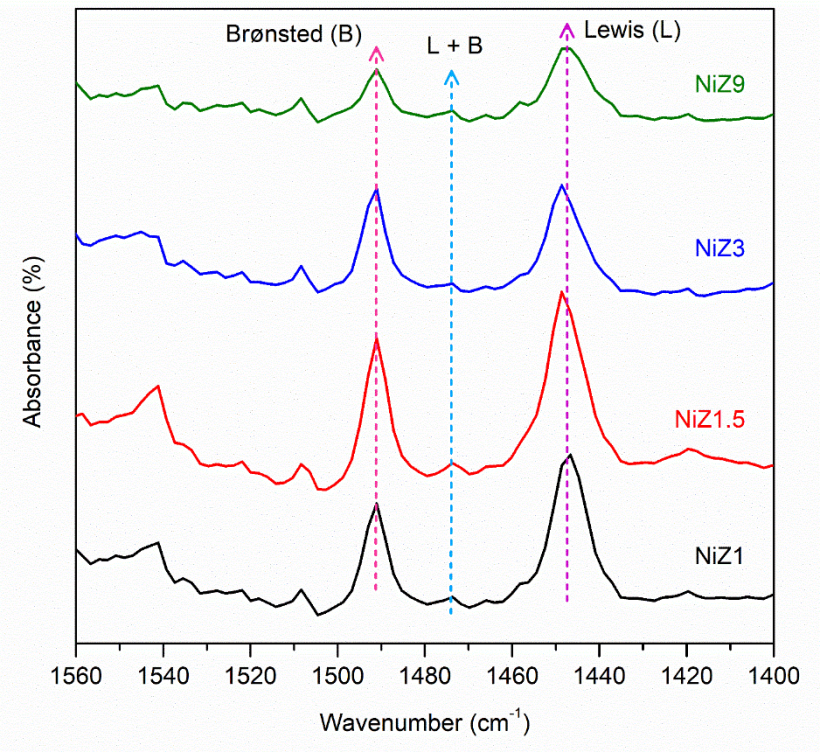

Figure 3 Pyridine-FTIR spectra of samples (m = 20 mg; $T_{analysis}$ = room temperature).

Table 1 Textural and acid properties of the NiZ catalyst.

Catalyst	S_{BET} (m^2g^{-1})	S_{meso} (m^2g^{-1})	S_{micro} (m^2g^{-1})	V_{meso} (cm^3g^{-1})	V_{micro} (cm^3g^{-1})	V_{total} (cm^3g^{-1})	Pore Diameter (nm)	Number of Acid sites (µmol g^{-1})		Ratio B/L	Lewis Density (µmol/m^2)
								Brønsted	Lewis		
NiZ1	209.81	178.57	31.24	0.245	0.015	0.260	4.89	22.62	123.04	0.1838	0.5865
NiZ1.5	341.98	266.73	75.25	0.331	0.026	0.357	2.61	32.93	151.87	0.2034	0.4441
NiZ3	210.41	180.27	30.14	0.293	0.012	0.305	9.36	16.15	87.13	0.1854	0.4141
NiZ9	158.06	138.32	19.74	0.244	0.014	0.258	3.75	9.69	50.18	0.2329	0.3174

On the basis of the data in **Table 1**, the Brønsted/Lewis acid ratios (B/L ratios) of NZ1 and NZ1.5 are lower than those of NiZ3 and NiZ9, demonstrating that NiZ1 and NiZ1.5 have greater amounts of weak acid and indicating that NiO particles are distributed in the zeolite pores. The results of the acidity analysis with pyridine FTIR are also consistent with the results of the H_2-TPR analysis, which are discussed in the next section. Acidity analysis using pyridine confirmed that the addition of NiO metal to the ZSM-5 support increased the number of Lewis and Brønsted acids.

N_2 adsorption-desorption analysis

The N_2 adsorption-desorption isotherms and pore size distributions of the NiZ catalyst are shown in **Figure 4**. All the catalysts exhibit combined type I and IV adsorption isotherms, which are characteristic of microporous and mesoporous hierarchical materials. At $P/P_0 < 0.1$, a low amount of N_2 is adsorbed to fill the micropores of the samples. N_2 molecules are subsequently diffused on the mesoporous layer, resulting in a considerable increase in N_2 adsorption. The condensation process leads to the formation of hysteresis loops, which are the characteristics of mesoporous materials [28].

Figure 4(a) shows that the NiZ1.5 catalyst has the greatest increase in N_2 adsorption at $P/P_0 < 0.1$ and P/P_0

= 0.1 - 0.4. The N_2 isotherm of the NiZ1.5 catalyst also exhibited a wide hysteresis loop at P/P_0 = 0.1 - 0.4 which is a characteristic of H4 mesoporous materials with varying pore size distributions [47]. Like the NiZ1.5 catalyst, the NiZ1 and NiZ3 catalysts showed N_2 isotherm adsorption at P/P_0 = 0.1 - 0.4 with approximately similar N_2 uptake, indicating a decrease in mesopores. The NiZ9 catalyst has the lowest N_2 absorption in the P/P_0 = 0.1 - 0.4 region, which implies that it has the fewest mesopores. Overall, the NiO/ZSM-5 catalyst has a smaller surface area than the ZSM-5 catalyst does (see ref. [41]) because of the presence of NiO. The surface areas of the NiZ1 to NiZ9 catalysts ranged from 341.98 to 158.06 m^2g^{-1}. The NiZ1 and NiZ1.5 catalysts have a broad mesoporous distribution with an intense incre

ase in N_2 adsorption volume, with a distribution ranging from 2.5 to 4.8 nm, as shown in **Figure 4(b)**, due to the formation of intraparticle mesoporous deposits. Data on the textural properties of the catalysts NiZ1, NiZ1.5, NiZ3, and NiZ9 are presented in **Table 1**.

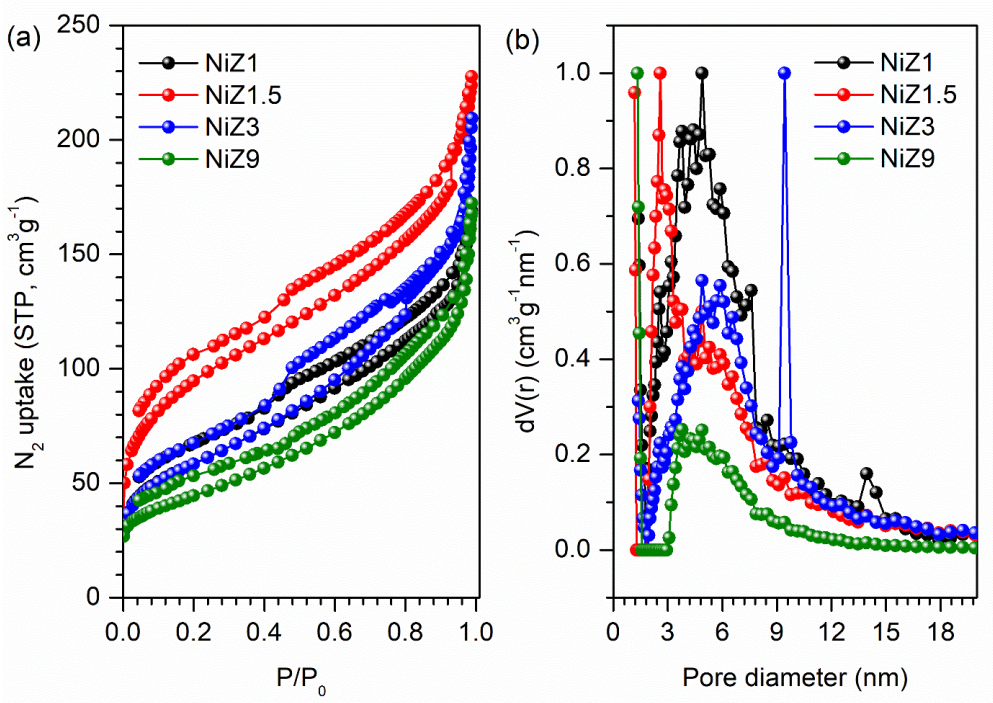

Figure 4 N_2 adsoprtion-desorption isotherm (a) and pore size distribution by DFT method (b) of catalyst ($T_{degasse}$ = 423 K; $T_{measured}$ = 77 K).

H_2-TPR study

H_2-TPR analysis provides information on the reducibility of NiO and the metal/support interactions. The H_2-TPR peak of reduced NiO can be classified into 3 types on the basis of the temperature range. The peak in the temperature region of 150 - 350 °C corresponds to a weak interaction between NiO and the support [48]. The second temperature region between 350 - 550 °C shows a moderate interaction between NiO and the support, and the third temperature region between 550 - 750 °C contains a peak, indicating a strong interaction between NiO and the support [49,50]. As depicted in **Figure 5**, all the catalysts exhibit an onset at 400 °C, implying that the NiZ catalysts could be reduced at temperatures higher than 400 °C. The NiZ1 catalyst shows 2 peaks centred at 511 and 672 °C due to the reduction of NiO into Ni metal. The reduction of NiO occurs in 2 stages: From Ni^{2+} to Ni^{+} and from Ni^{+} to Ni metal. The reduction peak with a relative high intensity at 672 °C indicates that the NiO particles are deposited in the mesopores of the supports [51]. The NiZ1.5 catalyst exhibited 3 peaks at maxima of 447, 513, and 653 °C, demonstrating moderate and strong interactions between NiO and ZSM-5. Nonetheless, the peak at 653 °C is stronger than the peaks at 447 and 513 °C, indicating that the strong interactions between NiO and

ZSM-5 are more dominant. This finding is also observed in the case of NiZ1. The H_2-TPR spectrum of NiZ3 has a similar pattern of peaks similar to that NiZ1.5. Unlike the other samples, NiZ9 exhibited multiple reduction peaks. The greater reduction peak for the NiZ1 catalyst than for the other catalysts at high temperatures ranging from 550 - 750 °C indicates that NiO is more evenly dispersed in the zeolite framework of the NiZ1 catalyst than in that of NiZ1.5. In addition, the occurrence of a small peak at 442 or 447 °C in NiZ1.5, NiZ3, and NiZ9 confirms the interaction reduction between NiO and ZSM-5 in NiZ1.5, NiZ3, and NiZ9. This result supports the XRD results, showing that NiO is more dispersed on NiZ1 via the generation of S–O–Ni by the ion exchange reaction during impregnation, which facilitates the strong interaction of NiO and ZSM-5 in NiZ1 compared with the other materials.

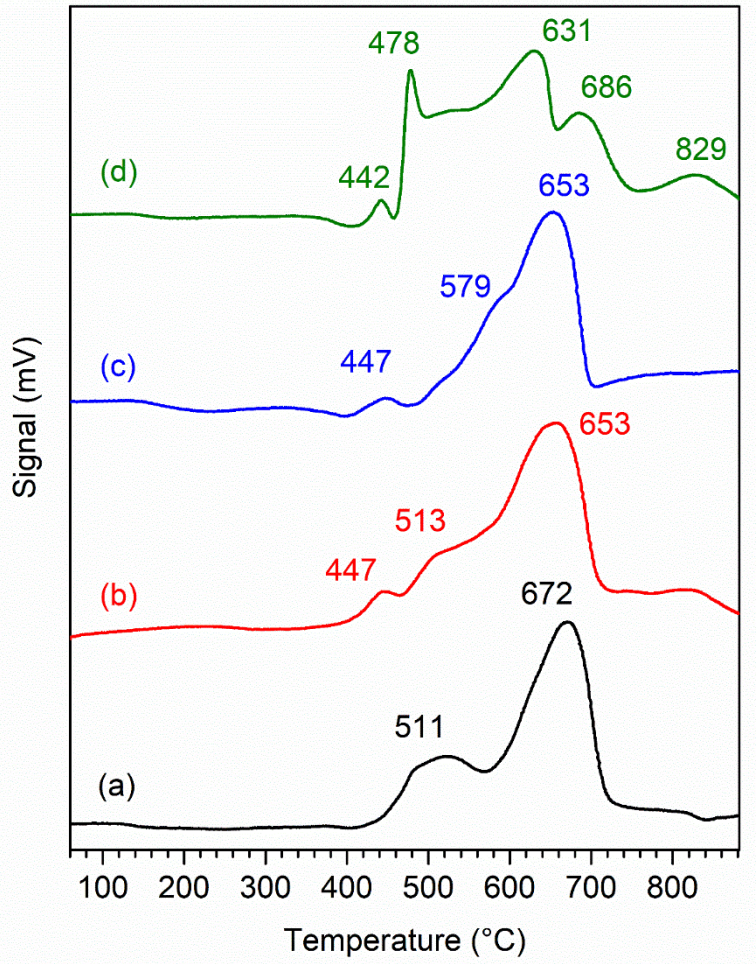

Figure 5 TPR Profile of NiZ1, NiZ1.5, NiZ3, and NiZ9 Catalyst (m = 200 mg; $T_{analysis}$ = 30 - 900 °C under H_2 flow).

Morphology analysis

SEM characterisation was used to determine the morphology and particle size of the NiZ catalysts. The morphologies of the synthesised NiZ catalysts with various supports Z1, Z1.5, Z3, and Z9 are shown in **Figure 6**. Notably, the NiZ1, NiZ1.5, NiZ3, and NiZ9 catalysts have similar morphologies. SEM characterisation of the catalyst revealed that Ni impregnation on the ZSM-5 supporting catalyst did not change the structure of ZSM-5. The results of this SEM analysis are consistent with the results of the XRD analysis. Data on the elemental composition of the NiO/ZSM5 catalyst from the EDX analysis results are presented in **Table 2**, which shows that the Si/Al ratio values range from the lowest value of 6.0 for the NiZ1 catalyst to approximately 9.3 for the NiZ1.5 catalyst.

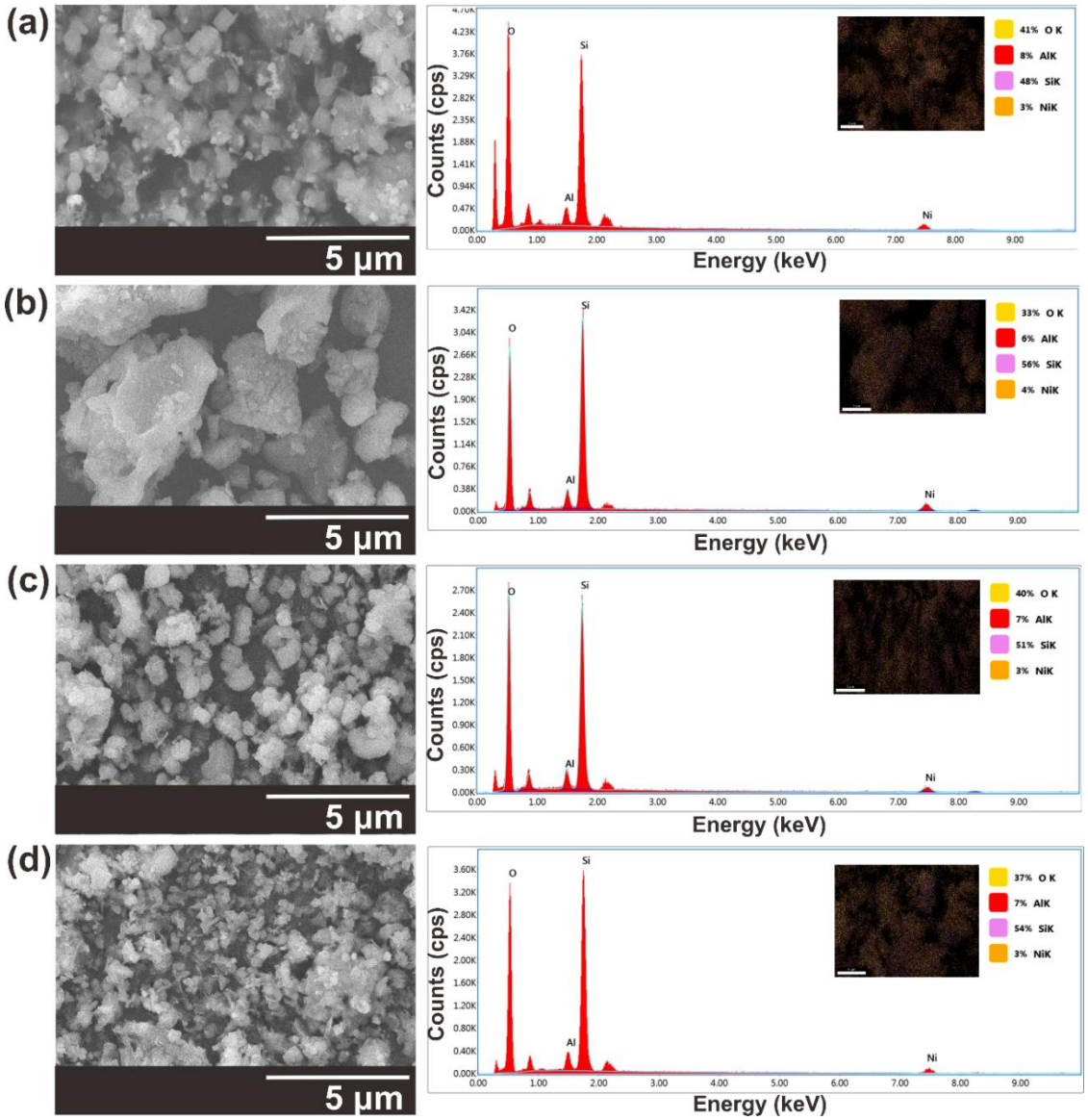

Figure 6 SEM micrograph and EDS spectra of (a) NiZ1, (b) NiZ1.5, (c) NiZ3, and (d) NiZ9 at magnification of 5,000× and acceleration voltage of 15 kV.

Table 2 Elemental composition of the NiZ1, NiZ1.5, NiZ3, and NiZ9 catalysts.

Catalyst	Elemental Composition (%w/w)				Ratio Si/Al
	Si	Al	O	Ni	
NiZ1	48	8	41	3	6.0
NiZ1.5	56	6	33	4	9.3
NIZ3	51	7	40	3	7.3
NiZ9	54	7	37	3	7.7

Moreover, TEM analysis of the NiZ1 and NiZ3 catalysts was performed to observe the nanostructure of the catalyst. The TEM images in **Figure 7** confirmed the formation of regular mesoporous channels with a hierarchical structure. TEM images of the NiZ1 catalyst show an even distribution of NiO particles on the catalyst support ZSM-5, as shown by H_2-TPR analysis and N_2 adsorption-desorption analysis. TEM analysis of the NiZ3 catalyst revealed a regular mesoporous channel shape with an approximate diameter of 3 nm.

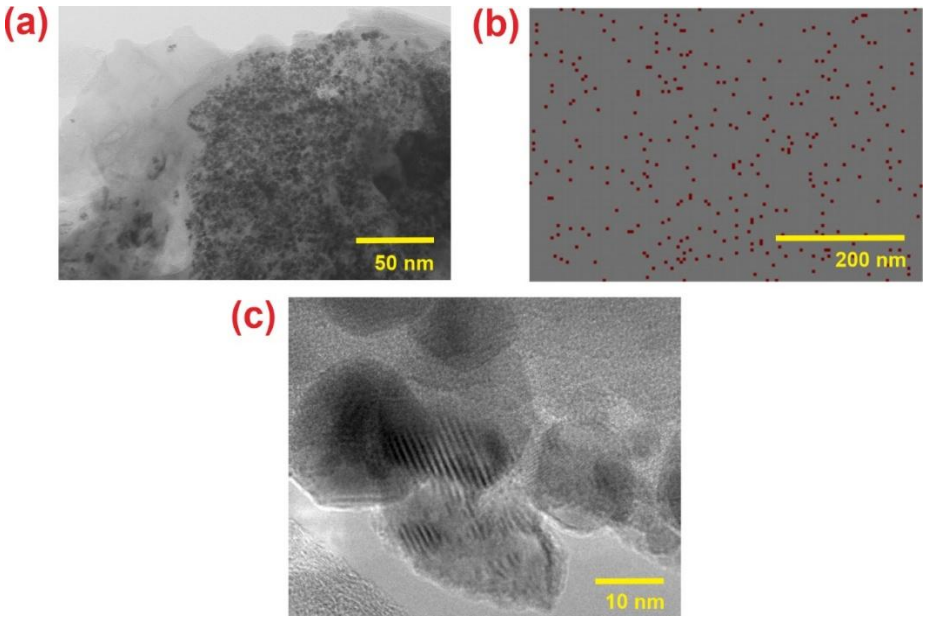

Figure 7 (a) TEM images of NiZ1 (at magnification of 100,000×) and (b) EDX spectrum of nickel in NiZ1. (c) is TEM images of NiZ3 with the existence of lattice fringes (at magnification of 200,000×).

XPS study

XPS analysis was performed to examine the oxidation state of elements in NiZ3. As depicted in **Figure 8**, the impregnation of Ni on Z3 increased the Ni 2*p* XPS spectrum. The Ni 2*p* XPS spectra show 4 prominent peaks. The Ni $2p_{3/2}$ peak and its satellite peak are prominent at a low BE, whereas the Ni $2p_{1/2}$ peak and its satellite peak arise at a high BE. The deconvolution results show that Ni $2p_{1/2}$ and Ni $2p_{3/2}$ yield 2 peaks associated with Ni^{3+} (854.4 eV for Ni $2p_{3/2}$ and 871.1 eV for Ni $2p_{1/2}$) and Ni^{2+} (852.3 eV for Ni $2p_{3/2}$ and 869.3 eV for Ni $2p_{1/2}$) [52]. Ni^{3+} is present because the charge transfer process, which is due to the presence of nickel vacancies (V_{Ni}) [53]. In addition, the presence of the Ni_2O_3 phase is minor compared with that of NiO in NiZ3, which cannot be confirmed by XRD. V_{Ni} can trap 2 electrons to generate V_{Ni}^{2-}, as presented in Eq. (1).

$$V_{Ni} \rightarrow V_{Ni}^{2+} + 2 \text{ holes} \quad (1)$$

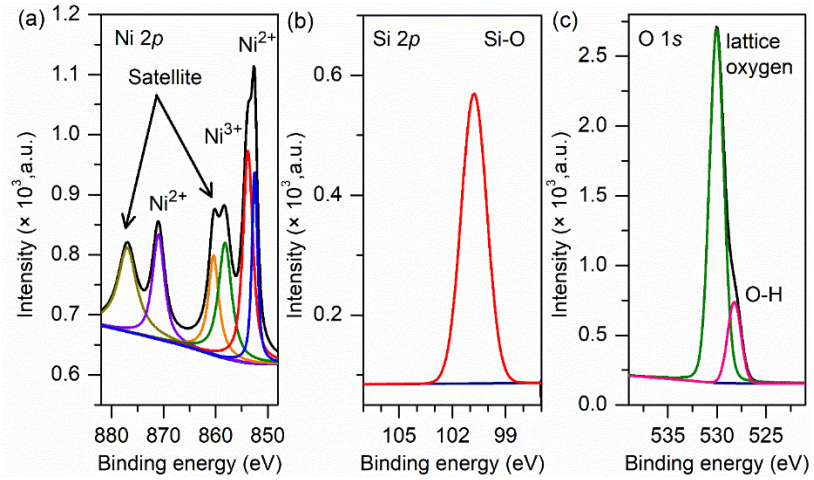

Figure 8 XPS Spectra of Oxygen (1s), Ni (2p) and Si (2p) of NiZ3 catalyst (using Mg Kα X-ray source with excitation energy output of 1,253.7 eV and a pass energy of 30 eV).

This process is accompanied by lattice relaxation, which increases the nearest neighbour distance. Consequently, the adjacent Ni^{2+} sites release an electron to generate a Ni^{3+} cation to compensate for the lattice relaxation due to the shorter distance of the Ni^{3+}–O^{2-} bond compared with the Ni^{2+}–O^{2-} bond [54]. Therefore, V_{Ni} and Ni^{3+} in NiZ3 because of the lattice relaxation induced by V_{Ni}^{2+} are balanced by the transition from the 2+ to the 3+ oxidation state for Ni [53].

The O 2s spectra exhibit 3 peaks after the deconvolution process. The peak at 529 eV arises from Ni–O bonds [55]. The Si–O bond is observed at 530 eV, which is approximately 2 eV lower than that reported in a previous study [48]. This comparison indicates that electron redistribution occurred, leading to the BE shifting. The peak at 531.5 eV is associated with the absorbed oxygen on the surface of NiZ3 [53]. However, the peak related to Ni_2O_3 is not observed, supporting the idea of charge balance, which is caused by lattice relaxation. In the Si 2*s* spectra, 2 prominent peaks are observed by deconvolution fitting and are attributed to the Si–O–Si and Si–O–H [56]. The absence of Si–O–Ni in both O 1*s* and Si 2*p* spectra reveals that the interaction between NiO and Z3 in NiZ3 is physical.

Catalytic deoxygenation of RTO

The hydrodeoxygenation reaction (HDO) of RTO with varying Ni contents on the ZSM-5 support was conducted in a semibatch reactor at 350 ℃ for 4 h, under a continuous 10% H_2/90% N_2 flow. As summarised in **Table 3**, the RTO was converted into 3 types of products: gas, liquid, and char. Among all the catalysts used, the NiZ1 and NiZ1.5 catalysts presented the highest conversion rates, approximately > 90%. In contrast, the conversion rates for NiZ3 and NiZ9 were slightly lower, reaching 82.13% and 83.37%, respectively. This difference is likely due to the relatively high acidity and large surface area of NiZ1 and NiZ1.5. However, these catalysts produced relatively high amounts of char, approximately 10.59% and 10.58%, respectively. In contrast, the use of NiZ3 and NiZ9 resulted in reduced char formation, at 4.95% and 1.76%, respectively. This outcome aligns with previous studies indicating that higher acidity can lead to secondary reactions that generate more polyaromatic compounds and promote coke formation on the ZSM-5 surface, ultimately leading to catalyst deactivation [57]. The liquid yield percentages ranged from 30% to 43.7%, with the highest yield achieved by NiZ1 (43.7%), followed by NiZ9, NiZ3, and NiZ1.5.

Table 3 Catalytic activity data of the NiZ1, NiZ1.5, NiZ3, and NiZ9 catalysts.

Catalyst	Conversion (%)	S_{gas}	S_{liquid}	S_{char}	DO Degree (%)
NiZ1	93.11	45.74	43.67	10.59	90.57
NiZ1,5	90.24	59.37	30.05	10.58	91.39
NiZ3	82.13	62.37	32.68	4.95	98.48
NiZ9	83.37	62.71	35.53	1.76	98.67

In general, the addition of NiO onto ZSM-5 increased the selectivity of the liquid product, yield and conversion of the HDO reaction of RTO compared with those of ZSM-5, as reported in our previous work [41]. Additionally, the coke composition resulting from the use of NiZ is also greater than that resulting from the use of ZSM-5 because the incorporation of NiO increases the number of catalytic acid sites. The higher level of acidity observed may result from the interaction between HMS and Ni, which facilitates the formation of Si–O–Ni species within the catalyst structure [58]. The acid sites play a role in breaking the C–C bond and initiating the coke formation on the catalyst surface [59]. The catalytic activity of the DO reaction can also be determined on the basis of the degree of DO. The degree of DO indicates the degree of effectiveness of DO reaction in converting the fatty acids in triglycerides into hydrocarbons [12]. The degree of DO represents the number of oxygenated species removed through the decarboxylation/-decarbonylation ($deCO_x$) reaction mechanism. The degree of DO reaches approximately 90% - 98.7% for all the catalysts. The degree of DO was greater than that of the ZSM-5 catalyst (see the data in our previous work [41]), which indicated that the

impregnation of Ni metal increased the catalytic activity of the conversion of RTO into biofuel because of the increased acidity and structural properties of the NiZ catalyst.

Selectivity of liquid hydrocarbon products from the HDO reaction

The composition of the liquid product was further analysed via GC-MS, as shown in **Figure 9**. According to the data, the main composition of the liquid product is hydrocarbon compounds with a selectivity range of 44% - 56%, followed by cyclic and aromatic hydrocarbons, carboxylic acids, ketones, and small amounts of alcohols. NiZ1 and NiZ3 exhibit higher hydrocarbon selectivity (56%) than do NiZ1.5 and NiZ9 (44%). This finding is attributed to the textural properties and acid sites of the catalysts. Furthermore, the highest selectivity of the cyclic compounds was observed with a 1.5 wt% Ni loading on the ZSM-5 support. This occurrence may be attributed to Brønsted acid sites that facilitate cyclisation reactions. These acidic sites promote C–C bond cleavage and subsequent cyclisation, leading to increased cyclic compound formation. These findings are consistent with previous studies on the DO of triolein [60]. A catalyst with a higher ZSM-5 crystallinity and the integration of textural properties and acid sites also produces more aromatic liquid products. The few acid sites in NiZ reduce the efficiency of NiZ9 for the HDO reaction. High mesoporous and catalyst acidity reduces coke formation, indicating good resistance to coke production. The incorporation of a higher loading of Ni onto the ZSM-5 support enhances decarboxylation and decarbonylation, consequently decreasing the selectivity towards carboxylic acids, thereby indicating that Ni functions as an effective catalyst in these reactions [58].

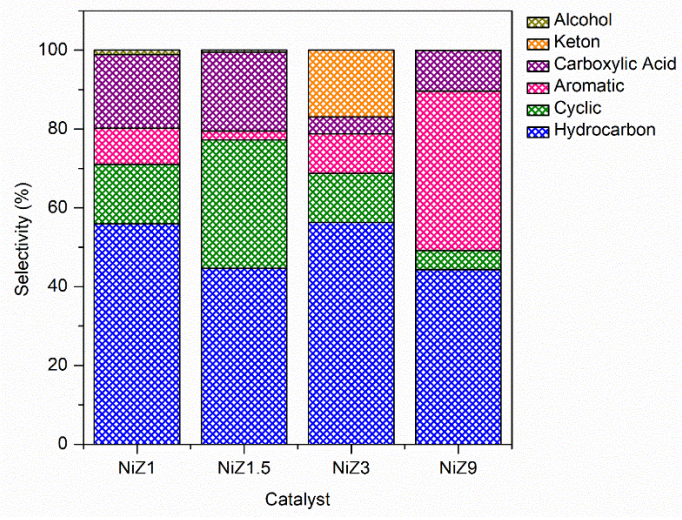

Figure 9 Distribution of compound type from liquid product of DO reaction using NiZ1, NiZ1.5, NiZ3, and NiZ9.

The composition of liquid hydrocarbon products resulting from the HDO reactions with NiZ1, NiZ1.5, NiZ3, and NiZ9 catalysts can be classified into gasoline, diesel, and long-chain hydrocarbons (heavy oils), as illustrated in **Figure 10**. The selectivity for diesel-range hydrocarbons varies from 8.75% to 82.79%, that for gasoline-range hydrocarbons varies from 0.81% to 20.63%, and that for heavy oils varies from 15.7% to 90.6%. Among the catalysts used, the NiZ3 catalyst achieved the highest selectivity for diesel-range hydrocarbons (82.7%). This result may be attributed to the predominant hierarchical structure of the Z3 support, which has a large mesopore diameter (9.36 nm). The high mesoporous diameter of NiZ3 integrated with high acid sites enhances the diffusion and mass transfer of long RTO molecules to the NiZ3 internal surface area, promoting the HDO conversion of RTO into diesel. In contrast, compared with other NiZ catalysts, the NiZ1.5 catalyst obtained the highest selectivity for long-chain hydrocarbon products at 90.2%. As previously summarised in **Table 1**, NiZ1.5 has the highest surface area, although its mesoporous diameter is relatively low

(2.61 nm). This small pore diameter leads to limited interactions between the catalyst and reactants due to the low diffusion of reactant molecules to the catalyst surface. Therefore, the pore size and structure of the catalyst play crucial roles in facilitating the diffusion of reactants, decomposition, and product formation within the catalyst pores, as well as in enabling the diffusion of products out of the pores [61].

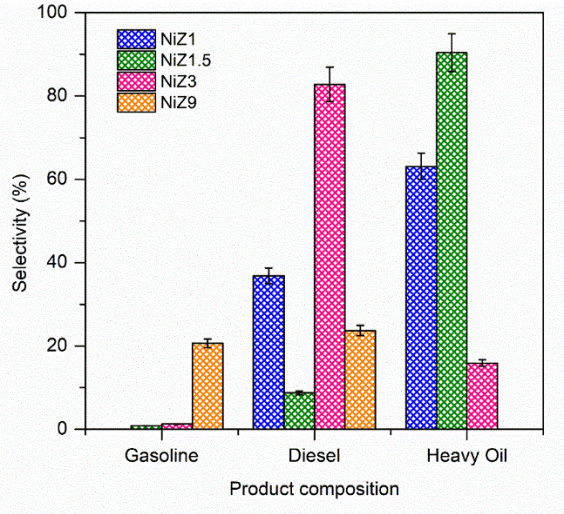

Figure 10 Selectivity of gasoline, diesel, and heavy oil.

In the HDO reaction with the NiZ catalyst, linear hydrocarbons C13–C22 were obtained with various alkane and alkene chain structures. The distributions of the alkane and alkene products for all the catalysts are shown in **Figure 11**. The NiZ1 and NiZ1.5 catalysts obtained a higher yields of alkane chains, whereas NiZ9 catalysts obtained higher yields of alkene chains. The selectivity between decarboxylation and decarbonylation over NiZ catalysts has been linked to the acidity of the support [62]. This finding indicates that the NiZ with higher acidity predominantly facilitates the formation of alkane hydrocarbons via a decarboxylation mechanism, whereas the NiZ catalyst with lower acidity is more inclined to produce alkene hydrocarbons through a decarbonylation reaction mechanism.

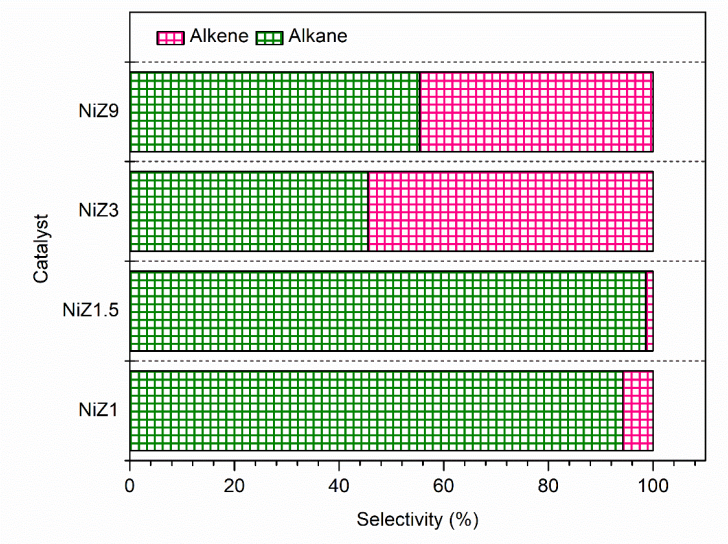

Figure 11 Hydrocarbon composition of liquid product using NiZ1, NiZ1.5, NiZ3, and NiZ9.

HDO reaction mechanism of the NiZ catalyst

The liquid product resulting from the HDO reaction was also characterised using FTIR analysis to provide information on the mechanism, as depicted in **Figure 12**. The FTIR spectrum of RTO and the liquid product of the catalyst shows the characteristic bands of RTO, including the –OH broad absorption band at 3,457 cm^{-1}, the –CH stretching aliphatic chain absorption band at approximately 2,922 cm^{-1}, the stretching –C=O ester band at 1,752 cm^{-1}, the C-O-C stretching band at 1,165 cm^{-1} and the alkane –CH and alkene =CH bending vibrations at 1,453 and 749 cm^{-1}, respectively. The –C=O (ester) and C-O-C (carbonyl) strain absorption bands, which are characteristic of the oxygenated species in triglycerides, are used to evaluate the mechanism of the HDO reaction [63]. A moderate shift in the strain vibration of the ester functional group –C=O in the liquid product from 1,752 cm^{-1} to 1,705 cm^{-1} (carboxylic acid group) was observed in the HDO reaction, indicating the dissociation of the ester bond to form a fatty acid intermediate [64]. More evidence of the removal of oxygenated compounds is the loss of the C–O–C stretching band at 1,165 cm^{-1} due to the elimination of the C–O–C unit from the carbonyl group in RTO. The use of NiZ1 and NiZ1.5 catalysts resulted in greater reduction of oxygenated compounds according to the small bands at 1,705 and 1,165 cm^{-1}, which was correlated with the strength of the acid sites and the hierarchical structure of the catalyst. The NiZ9 catalyst exhibited a weaker acidity strength and weaker intensity of the –C=O stretching band from the ester group [65]. The results of the FTIR analysis indicate that the initial stage of the reaction involves the transformation of triglycerides into fatty acids in the presence of an acid catalyst. As the reaction time increased, the peak intensity of –C=O decreased, indicating the elimination of carboxylic fragments in free fatty acids, which then formed hydrocarbons.

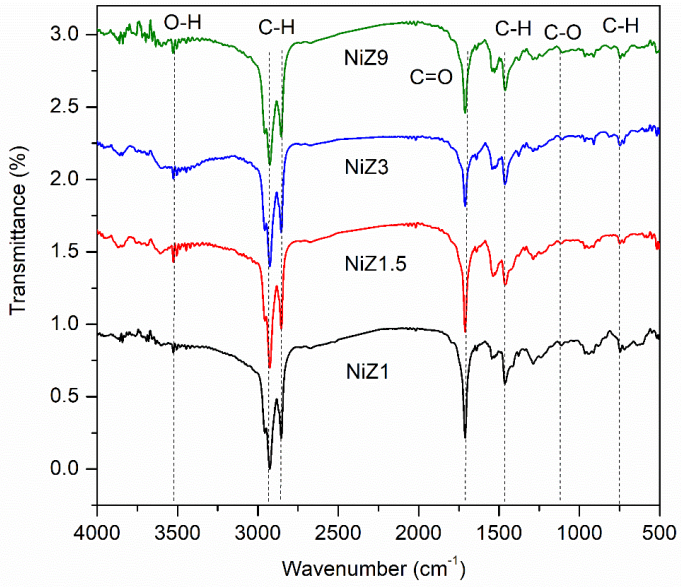

Figure 12 FTIR spectra of liquid product using NiZ1, NiZ1,5, NiZ3, and NiZ9. The samples were measured at wavenumber of 4,000 - 400 cm^{-1}.

In detail, we proposed the mechanism for the DO reaction of RTO, as shown in **Figure 13**. In the initial stage, β-elimination of RTO occurs to form a series of fatty acids, including palmitic acid, linoleic acid, oleic acid, and stearic acid. A high amount of acid and high micromesoporosity (NiZ1 and NiZ1.5) lead to the polymerization of fatty acids to generate hydrocarbons ranging from C_{20}–C_{26} (heavy oils). The distribution of NiO particles in the mesoporous structure may cover the ZSM-5 pores, thereby reducing the effectiveness of the cracking reaction. The moderate acid and moderate mesoporosity of NiZ3 promote the generation of 1-pentadecene and 1-heptadecene via a decarbonylation reaction. Subsequently, isomerization produces 3-tridecene and 8-heptadecene, which is followed by cracking and aromatisation to yield benzene. These

features also lead to the decarboxylation of fatty acids into pentadecane and heptadecane. These compounds are also produced via the hydrogenation of 1-pentadecene and 1-heptadecene (which results from decarbonylation). Furthermore, the C–C cracking occurs to transform pentadecane and heptadecane into tridecane and undecane. The products resulting from application of NiZ3 are categorised as diesel hydrocarbons. NiZ9, with low acid and low mesoporosity features, converts fatty acids into tetradecane and hexadecane, which is more feasible for transformation into decane and dodecane. A high composition of decane and dodecane is classified as gasoline hydrocarbons. To produce green renewable energy, such as green diesel, the synergy of the number of acid sites and micromesoporous features must be regulated to facilitate the conversion of RTO into green diesel. This alteration can be performed by controlling these features during synthesis or controlling the amount of NiO to provide acid sites.

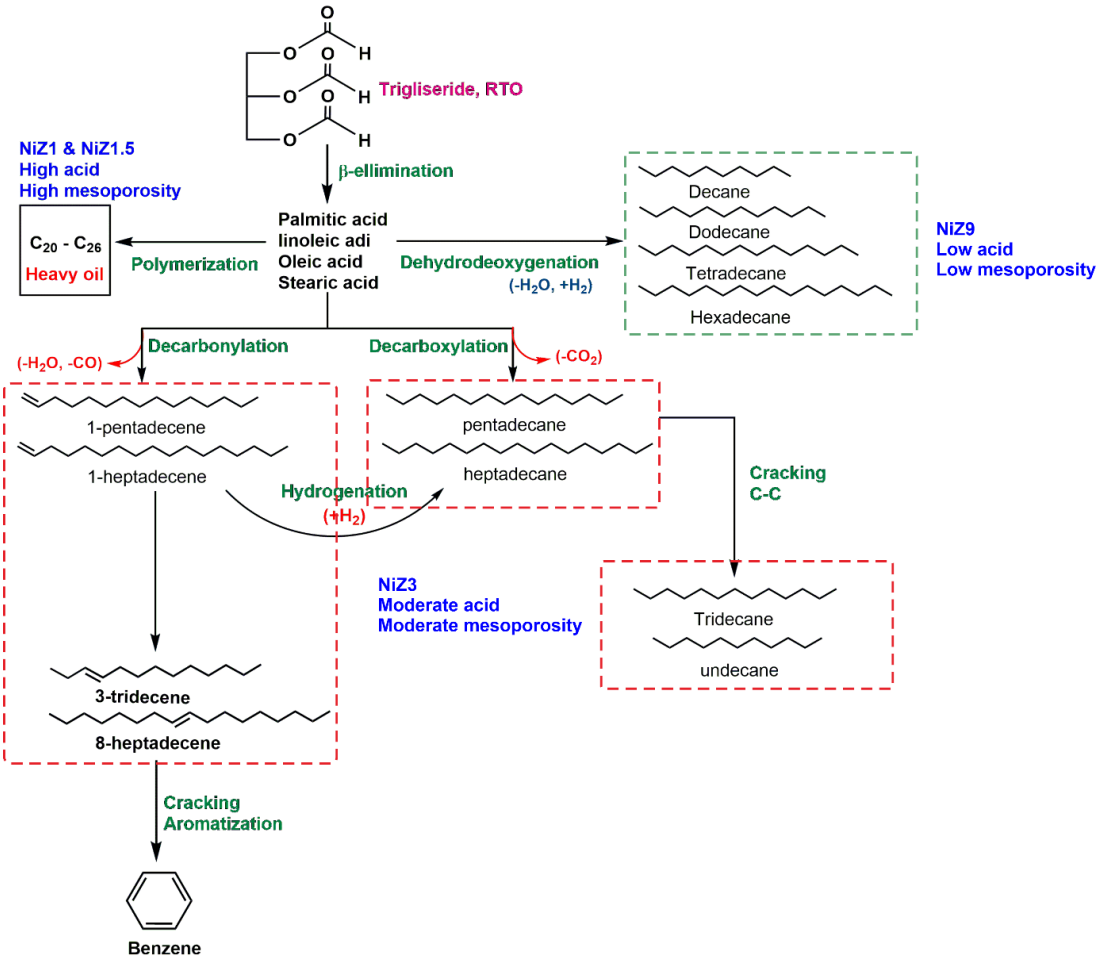

Figure 13 Mechanism of DO reaction using NiZ1, NiZ1.5, NiZ3, and NiZ9.

Comparison studies

Comparing studies with other works is very valuable for comparing the resulting data with reported data. As shown in **Table 4**, various catalysts, feedstocks, and reaction conditions affect hydrocarbons selectivity and diesel selectivity. The absence of Ni species on CaO requires a longer reaction time to generate a range of diesel hydrocarbons from waste cooking oil (WCO). Notably, compared with the other catalysts, NiZ3 (in this work) has the highest diesel selectivity at 4 h of reaction with RTO as a feedstock, which is greater than that of 15Ni/Al-MCM-41. This finding confirms that the presence of Ni species on the support catalyst is feasible for improving the diesel generation from oil feedstock. Nonetheless, the hydrocarbon selectivity of NiZ3 is lower than that of 15Ni/Al-MCM-41, whereas the diesel

selectivity is richer than that of 15Ni/Al-MCM-41. In addition to different reaction conditions, such features of NiZ3, including moderate micromesoporosity and moderate acid sites, facilitate the generation of diesel compared with 15Ni/Al-MCM-41, which has high mesoporosity and acid sites. The combination of a transition metal and ZSM-5 shows varying hydrocarbon selectivity depending on the feedstock. The hydrocarbon selectivity of NiZ3 (our work) is comparable to that of Ni-Ce/ZSM-5 and Co-H-ZSM, but lower than that of Fe/ZSM-5/SAPO-11 and NiFe/ZSM-5/SAPO-11. However, the green diesel selectivity of NiZ3 is lower than that of Ni-Ce/ZSM-5. This finding relates to the reaction conditions, especially the reaction pressure, which affects the reaction process. The reaction temperature also affects the hydrocarbon selectivity as reported by Jovita *et al.* [66], showing the hydrocarbon selectivity of 96% using NiO/mesoporous aluminosilicate when the reaction temperature set at 380 °C [66]. Nonetheless, the presence of another transition metal (Ce) in Ni-Ce/ZSM-5 improves green diesel selectivity. It can be noted that the diesel selectivity of NiZ3 can be further improved by controlling reaction conditions, adding catalytic sites, and adding other transition metals to achieve high diesel selectivity for future green renewable energy generation and address energy issues.

Table 4 Comparative studies of the DO reaction for diesel generation.

Catalyst	Feedstock	Reaction Condition	Hydrocarbon Selectivity (%)	Diesel Selectivity (%)	Ref.
CaO	Waste cooking oil	t = 6 h; T = 400 °C; under N_2 flow	84	76	[67]
10% Ni-Fe/SBA-15	Waste cooking oil	t = 2 h; T = 350 °C; under N_2 flow	73	57	[68]
20% Ni/AC	Waste cooking oil	t = 3 h; T = 350 °C; under N_2 flow	87	77	[69]
CoW/SiO_2-Al_2O_3	Tung oil	t = 2 h; T = 350 °C; under N_2 flow	69	30	[70]
15Ni/Al-MCM-41	RTO	t = 4 h; T = 350 °C; under N_2 flow	60	62	[71]
NiMo/ZSM-5	Soybean oil	t = 4 h; T = 380 °C; under H_2 flow	-	79	[72]
Ni-Ce/ZSM-5	Mixed plastic waste	t = 6 h; T = 300 °C; p = 70 bar, under H_2 flow	59	95	[73]
Fe/ZSM-5/SAPO-11	Palm oil	t = 2 h; T = 300 °C; p = 60 bar, under H_2 flow	79	-	[74]
NiFe/ZSM-5/SAPO-11	Palm oil	t = 2 h; T = 300 °C; p = 60 bar, under H_2 flow	81	-	[74]
Co/H-ZSM-5	Stearic acid	t = 2 h; T = 260 °C; p = 30 bar under H_2 flow	60	-	[75]
NiZ3	RTO	t = 4 h; T = 350 °C; under H_2/N_2 flow (ratio of H_2/N_2 = 1/9)	56	83	This work

Conclusions

The control of the crystallisation time during the synthesis of ZSM-5 affects the microporous and mesoporous features. Additionally, the incorporation of NiO on the ZSM-5 surface resulting from different crystallisation times results in different dispersals of NiO on ZSM-5, affecting various acid sites. Increasing the crystallisation time decreases the microporous and mesoporous properties of ZSM-5. Consequently, the interaction between NiO and ZSM-5 decreases according to the XRD results, decreasing the number of acid sites. The synergy between micromesoporous features and acid sites results in different major products from the DO reaction of RTO. The high micromesoporous properties and acid sites generate heavy oil products (> C20), whereas the moderate and low compositions of micromesoporous features and acid sites are more feasible for producing green diesel and gasoline products, respectively. According to these results, NiZ3 is effective at producing green diesel hydrocarbons. This finding shows that altering these properties is beneficial for generating a high level of

diesel hydrocarbon, which can be used for other oil feedstocks to obtain insights into scaling-up processes in the future.

Acknowledgements

The authors would like to acknowledgement the Ministry of Education, Culture, Research and Technology, Indonesia for the financial support under Doctoral Dissertation Research (PDD) research grant with contract number of 1925/PKS/ITS/2023.

Declaration of generative AI in scientific writing

The authors acknowledge the use of generative AI tools (Grammarly) in the preparation of this manuscript, specifically for language editing and grammar correction. No content generation or data interpretation was performed by AI. The authors take full responsibility for the content and conclusions of this work

CRediT author statement

Dina Kartika Maharani: Writing–original draft, Methodology, Conceptualization, Investigation. **Riki Subagyo:** Writing–review & editing, Visualization. **Stella Jovita:** Writing–review & editing. **Khawiyatur Rivah Agustina:** Formal Analysis. **Hasliza Bahruji:** Writing–review & editing, Data Curation, Validation. **Reva Edra Nugraha:** Formal Analysis. **Nurul Asikin Mijan:** Formal Analysis. **Aishah Abdul Jalil:** Writing–review & editing. **Didik Prasetyoko:** Writing–review & editing, Supervision, Validation. **Yuly Kusumawati:** Writing–review & editing, Funding Acquisition, Supervision.

References

[1] Y Nakagawa, M Tamura and K Tomishige. Recent development of production technology of diesel- and jet-fuel-range hydrocarbons from inedible biomass. *Fuel Processing Technology* 2019; **193**, 404-422.

[2] WC Wang and L Tao. Bio-jet fuel conversion technologies. *Renewable Sustainable Energy Reviews* 2016; **53**, 801-822.

[3] AY Khodakov, W Chu and P Fongarland. Advances in the development of novel cobalt Fischer-Tropsch catalysts for synthesis of long-chain hydrocarbons and clean fuels. *Chemical Reviews* 2007; **107**, 1692-1744.

[4] K Littlewood. Gasification: Theory and application. *Progress in Energy and Combustion Science* 1977; **3(1)**, 35-71.

[5] EG Pereira, JN da Silva, JL de Oliveira and CS Machado. Sustainable energy: A review of gasification technologies. *Renewable and Sustainable Energy Reviews* 2012; **16(7)**, 4753-4762.

[6] M Ameen, MT Azizan, A Ramli, S Yusup and MS Alnarabiji. Catalytic hydrodeoxygenation of rubber seed oil over sonochemically synthesized Ni-Mo/γ-Al_2O_3 catalyst for green diesel production. *Ultrasonics Sonochemistry* 2019; **51**, 90-102.

[7] AA Mancio, SAP da Mota, CC Ferreira, TUS Carvalho, OS Neto, JR Zamian, ME Araújo, LEP Borges and NT Machado. Separation and characterization of biofuels in the jet fuel and diesel fuel ranges by fractional distillation of organic liquid products. *Fuel* 2018; **215**, 212-225.

[8] YW Cheah, MA Salam, J Sebastian, S Ghosh, O Öhrman, D Creaser and L Olsson. Thermal annealing effects on hydrothermally synthesized unsupported MoS_2 for enhanced deoxygenation of propylguaiacol and kraft lignin. *Sustainable Energy Fuels* 2021; **5(20)**, 5270-5286.

[9] PE Ruiz, BG Frederick, WJ De Sisto, RN Austin, LR Radovic, K Leiva, R García, N Escalona and MC Wheeler. Guaiacol hydrodeoxygenation on MoS_2 catalysts: Influence of activated carbon supports. *Catalysis Communications* 2012; **27**, 44-48.

[10] A Gutierrez, EM Turpeinen, TR Viljava and O Krause. Hydrodeoxygenation of model compounds on sulfided CoMo/γ-Al_2O_3 and NiMo/γ-Al_2O_3 catalysts; Role of sulfur-containing groups in reaction networks. *Catalysis Today* 2017; **285**, 125-134.

[11] YW Cheah, MA Salam, J Sebastian, S Ghosh, P Arora, O Öhrman, L Olsson and D Creaser. Upgrading of triglycerides, pyrolysis oil, and lignin over metal sulfide catalysts: A review on the reaction mechanism, kinetics, and catalyst deactivation. *Journal of Environmental Chemical Engineering* 2023; **11(3)**, 109614.

[12] D Kubička, J Horáček, M Setnička, R Bulánek, A

Zukal and I Kubičková. Effect of support-active phase interactions on the catalyst activity and selectivity in deoxygenation of triglycerides. *Applied Catalysis B: Environmental* 2014; **145**, 101-107.

[13] MY Smirnova, OV Kikhtyanin, MY Smirnov, AV Kalinkin, AI Titkov, AB Ayupov and DY Ermakov. Effect of calcination temperature on the properties of Pt/SAPO-31 catalyst in one-stage transformation of sunflower oil to green diesel. *Applied Catalysis A: General* 2015; **505**, 524-531.

[14] MO Bengoechea, A Hertzberg, N Miletić, PL Arias and T Barth. Simultaneous catalytic de-polymerization and hydrodeoxygenation of lignin in water/formic acid media with Rh/Al_2O_3, Ru/Al_2O_3 and Pd/Al_2O_3 as bifunctional catalysts. *Journal of Analytical and Applied Pyrolysis* 2015; **113**, 713-722.

[15] X Wang, P Wu, Z Wang, L Zhou, Y Liu, H Cheng, M Arai, C Zhang and F Zhao. Chlorine-modified Ru/TiO_2 catalyst for selective guaiacol hydrodeoxygenation. *ACS Sustainable Chemistry & Engineering* 2021; **9(8)**, 3083-3094.

[16] R Shu, B Lin, J Zhang, C Wang, Z Yang and Y Chen. Efficient catalytic hydrodeoxygenation of phenolic compounds and bio-oil over highly dispersed Ru/TiO_2. *Fuel Processing Technology* 2019; **184**, 12-18.

[17] TC Hoff, R Thilakaratne, DW Gardner, RC Brown and JP Tessonnier. Thermal stability of aluminum-rich ZSM-5 zeolites and consequences on aromatization reactions. *The Journal of Physical Chemistry C* 2016; **120(36)**, 20103-20113.

[18] L Treps, A Gomez, T de Bruin and C Chizallet. Environment, stability and acidity of external surface sites of Silicalite-1 and ZSM-5 micro and nano slabs, sheets, and crystals. *ACS Catalysis* 2020; **10(5)**, 3297-3312.

[19] KA Tarach, J Martinez-Triguero, F Rey and K Góra-Marek. Hydrothermal stability and catalytic performance of desilicated highly siliceous zeolites ZSM-5. *Journal of Catalysis* 2016; **339**, 256-269.

[20] PA Alaba, YM Sani, IY Mohammed, YA Abakr and WMAW Daud. Synthesis and application of hierarchical mesoporous HZSM-5 for biodiesel production from shea butter. *Journal of the Taiwan Institute of Chemical Engineers* 2016; **59**, 405-412.

[21] F Goodarzi, IP Herrero, GN Kalantzopoulos, S Svelle, A Lazzarini, P Beato, U Olsbye and S Kegnæs. Synthesis of mesoporous ZSM-5 zeolite encapsulated in an ultrathin protective shell of silicalite-1 for MTH conversion. *Microporous and Mesoporous Materials* 2020; **292**, 109730.

[22] S Moon, HJ Chae and MB Park. Oligomerization of light olefins over ZSM-5 and beta zeolite catalysts by modifying textural properties. *Applied Catalysis A: General* 2018; **553**, 15-23.

[23] Y Ji, H Yang and W Yan. Strategies to enhance the catalytic performance of ZSM-5 zeolite in hydrocarbon cracking: A review. *Catalysts* 2017; **7(12)**, 367.

[24] J Zhang, L Wang, Y Ji, F Chen and FS Xiao. Mesoporous zeolites for biofuel upgrading and glycerol conversion. *Frontier of Chemical Science and Engineering* 2018; **12**, 132-144.

[25] J Wang, Z Zhong, K Ding, B Zhang, A Deng, M Min, P Chen and R Ruan. Successive desilication and dealumination of HZSM-5 in catalytic conversion of waste cooking oil to produce aromatics. *Energy Conversion and Management* 2017; **147**, 100-107.

[26] DV Peron, VL Zholobenko, JHS de Melo, M Capron, N Nuns, MO de Souza, LA Feris, NR Marcilio, VV Ordomsky and AY Khodakov. External surface phenomena in dealumination and desilication of large single crystals of ZSM-5 zeolite synthesized from a sustainable source. *Microporous and Mesoporous Materials* 2019; **286**, 57-64.

[27] I Qoniah, D Prasetyoko, H Bahruji, S Triwahyono, AA Jalil, Suprapto, Hartati and TE Purbaningtias. Direct synthesis of mesoporous aluminosilicates from Indonesian kaolin clay without calcination. *Applied Clay Science* 2105; **118**, 290-294.

[28] H Tehubijuluw, R Subagyo, MF Yulita, RE Nugraha, Y Kusumawati, H Bahruji, AA Jalil, H Hartati and D Prasetyoko. Utilization of red mud waste into mesoporous ZSM-5 for methylene blue adsorption-desorption studies. *Environmental Science and Pollution Research* 2021; **28**, 37354-37370.

[29] W Li, F Li, H Wang, M Liao, P Li, J Zheng, C Tu

and R Li. Hierarchical mesoporous ZSM-5 supported nickel catalyst for the catalytic hydrodeoxygenation of anisole to cyclohexane. *Molecular Catalysis* 2020; **480**, 110642.

[30] Y Wang, H Huang, NC Baxter, Y Liao, Y Zhao and S Wang. Guaiacol hydrodeoxygenation over Pd catalyst with mesoporous ZSM-5 support synthesized by solid-state crystallization. *Catalysis Today* 2020; **358**, 60-67.

[31] S Chen, G Zhou and C Miao. Green and renewable bio-diesel produce from oil hydrodeoxygenation: Strategies for catalyst development and mechanism. *Renewable and Sustainable Energy Reviews* 2019; **101**, 568-589.

[32] N Hongloi, P Prapainainar and C Prapainainar. Review of green diesel production from fatty acid deoxygenation over Ni-based catalysts. *Molecular Catalysis* 2022; **523**, 111696.

[33] X Yu and CT Williams. Recent applications of nickel and nickel-based bimetallic catalysts for hydrodeoxygenation of biomass-derived oxygenates to fuels. *Catalysis Science and Technology* 2023; **13(3)**, 802-825.

[34] EF Iliopoulou, SD Stefanidis, KG Kalogiannis, A Delimitis, AA Lappas and KS Triantafyllidis. Catalytic upgrading of biomass pyrolysis vapors using transition metal-modified ZSM-5 zeolite. *Applied Catalysis B: Environmental* 2012; **127**, 281-290.

[35] JA Botas, DP Serrano, A García, J de Vicente and R Ramos. Catalytic conversion of rapeseed oil into raw chemicals and fuels over Ni- and Mo-modified nanocrystalline ZSM-5 zeolite. *Catalysis Today* 2012; **195(1)**, 59-70.

[36] W Li, H Wang, X Wu, LE Betancourt, C Tu, M Liao, X Cui, F Li, J Zheng and R Li. Ni/hierarchical ZSM-5 zeolites as promising systems for phenolic bio-oil upgrading: Guaiacol hydrodeoxygenation. *Fuel* 2020; **274**, 117859.

[37] S Li, L Guo, X He, C Qiao and Y Tian. Synthesis of uniform Ni nanoparticles encapsulated in ZSM-5 for selective hydrodeoxygenation of phenolics. *Renewable Energy* 2022; **194**, 89-99.

[38] X Huang, C Wang, Y Zhu, W Xu, Q Sun, A Xing, L Ma, J Li, Z Han and Y Wang. Facile synthesis of ZSM-5 nanosheet arrays by preferential growth over MFI zeolite [100] face for methanol conversion. *Microporous and Mesoporous Materials* 2019; **288**, 109573.

[39] Z Ma, X Wang, X Ma, M Tan, G Yang and Y Tan. Catalytic roles of acid property in different morphologies of H-ZSM-5 zeolites for syngas-to-aromatics conversion over $ZnCrO_x$/H-ZSM-5 catalysts. *Microporous and Mesoporous Materials* 2023; **349**, 112420.

[40] H Cui, X Yan, B Liu, X Zhao, X Zhang, X Zhao, X Tong, Y Wang and Y Xing. Flower-like spherical Ni-benzimidazole derived Ni-NiO-C complexed with carbon nanotubes as electrocatalysts for lithium-sulfur battery. *Journal of Alloys and Compounds* 2023; **931**, 167402.

[41] DK Maharani, Y Kusumawati, WN Safitri, RE Nugraha, H Holilah, NA Sholeha, AA Jalil, H Bahruji and D Prasetyoko. Optimization of hierarchical ZSM-5 structure from kaolin as catalysts for biofuel production. *RSC Advances* 2023; **13(21)**, 14236-14248.

[42] C Hu, C Fang, Y Lu, Y Wang, J Chen and M Luo. Selective oxidation of diethylamine on CuO/ZSM-5 catalysts: the role of cooperative catalysis of CuO and surface acid sites. *Industrial & Engineering Chemistry Research* 2020; **59(20)**, 9432-9439.

[43] T Pan, S Ge, M Yu, Y Ju, R Zhang, P Wu, K Zhou and Z Wu. Synthesis and consequence of Zn modified ZSM-5 zeolite supported Ni catalyst for catalytic aromatization of olefin/paraffin. *Fuel* 2022; **311**, 122629.

[44] Q A'yuni, A Rahmayanti, H Hartati, P Purkan, R Subagyo, S Fuadah, NA Sholeha, H Bahruji and H Hikmat. Transforming volcanic mud into mesoporous silica xerogel and its performance for efficient humidity adsorption. *Journal of Saudi Chemical Society* 2023; **27(6)**, 101771.

[45] Y Cui, B Chen, L Xu, M Chen, C Wu, J Qiu, G Cheng, N Wang, J Xu and X Hu. CO_2 methanation over the Ni-based catalysts supported on the hollow ZSM-5 zeolites: Effects of the hollow structure and alkaline treatment. *Fuel* 2023; **334**, 126783.

[46] H Wang, S Wang, L Guo, C Qiao and Y Tian. Hierarchical ZSM-5 supported Ni catalysts for hydrodeoxygenation of phenolics: Effect of reactant volumes and substituents. *Chemical*

Engineering Journal 2023; **455**, 140647.

[47] B Velaga, R Doley and NR Peela. Rapid synthesis of hierarchical ZSM-5 zeolites for the reactions involving larger reactant molecules. *Advanced Powder Technology* 2021; **32(4)**, 1033-1046.

[48] RK Sharma, G Dey, P Banerjee, JP Maity, CM Lu, SC Wang, YH Huang, PY Lin, YP Chen and CY Chen. Influence of chemical and bio-surfactants on physiochemical properties in mesoporous silica nanoparticles synthesis. *Journal of Materials Research and Technology* 2023; **24**, 2629-2639.

[49] TV Sagar, N Sreelatha, G Hanmant, M Surendar, N Lingaiah, KSR Rao, CVV Satyanarayana, IAK Reddy and PSS Prasad. Influence of method of preparation on the activity of La–Ni–Ce mixed oxide catalysts for dry reforming of methane. *RSC Advances* 2014; **4(91)**, 50226-50232.

[50] X Wen, L Xu, M Chen, Y Shi, C Lv, Y Cui, X Wu, G Cheng, C Wu, Z Miao, F Wang and X Hu. Exploring the influence of nickel precursors on constructing efficient Ni-based CO_2 methanation catalysts assisted with in-situ technologies. *Applied Catalysis B: Environmental* 2021; **297**, 120486.

[51] L Wei, W Haije, N Kumar, J Peltonen, M Peurla, H Grenman and W de Jong. Influence of nickel precursors on the properties and performance of Ni impregnated zeolite 5A and 13X catalysts in CO_2 methanation. *Catalysis Today* 2021; **362**, 35-46.

[52] C Alex, G Shukla and NS John. Introduction of surface defects in NiO with effective removal of adsorbed catalyst poisons for improved electrochemical urea oxidation. *Electrochimica Acta* 2021; **385**, 138425.

[53] YJ Lin, TH Su, PC Kuo and HC Chang. A source of free holes in NiO thin films with different nickel content that are prepared using the sol-gel method. *Materials Chemistry and Physics* 2022; **276**, 125345.

[54] P Dubey, N Kaurav, RS Devan, GS Okram and YK Kuo. The effect of stoichiometry on the structural, thermal and electronic properties of thermally decomposed nickel oxide. *RSC Advances* 2018; **8(11)**, 5882-5890.

[55] HT Handal, WAA Mohamed, AA Labib, SA Moustafa and AA Sery. The influence of surface modification on the optical and capacitive properties of NiO nanoparticles synthesized via surfactant-assisted coprecipitation. *Journal of Energy Storage* 2021; **44**, 103321.

[56] R Subagyo, GR Anindika, DI Utami, WS Sarifuddin, L Zhang, S Jovita, KR Agustina, NA Mijan, Y Zetra, H Bahruji, D Suhendar, FA Mawaddah, D Prasetyoko, SZ Bisri, Arramel and Y Kusumawati. Dendritic fibrous nano silica-titania for high-performance photocatalytic hydrogen evolution. *ACS Applied Energy Materials* 2025; **8(3)**, 1598-1608.

[57] N Chaihad, S Karnjanakom, A Abudula and G Guan. Zeolite-based cracking catalysts for bio-oil upgrading: A critical review. *Resources Chemicals and Materials* 2022; **1(2)**, 167-183.

[58] S Zulkepli, JC Juan, HV Lee, NSA Rahman, PL Show and EP Ng. Modified mesoporous HMS supported Ni for deoxygenation of triolein into hydrocarbon-biofuel production. *Energy Conversion and Management* 2018; **165**, 495-508.

[59] RS Tan, TAT Abdullah, SA Mahmud, R Md Zin and K Md Isa. Catalytic steam reforming of complex gasified biomass tar model toward hydrogen over dolomite promoted nickel catalysts. *International Journal of Hydrogen Energy* 2019; **44(39)**, 21303-21314.

[60] S Zulkepli, HV Lee, NA Rahman, LT Chuan, PL Show, WH Chen and JC Juan. Highly active iron-promoted hexagonal mesoporous silica (HMS) for deoxygenation of triglycerides to green hydrocarbon-like biofuel. *Fuel* 2022; **308**, 121860.

[61] Nishu, R Liu, MM Rahman, M Sarker, M Chai, C Li and J Cai. A review on the catalytic pyrolysis of biomass for the bio-oil production with ZSM-5: Focus on structure. *Fuel Processing Technology* 2020; **199**, 106301.

[62] M Žula, M Grilc and B Likozar. Hydrocracking, hydrogenation and hydro-deoxygenation of fatty acids, esters and glycerides: Mechanisms, kinetics and transport phenomena. *Chemical Engineering Journal* 2022; **444**, 136564.

[63] MS Gamal, N Asikin-Mijan, M Arumugam, U Rashid and YH Taufiq-Yap. Solvent-free catalytic deoxygenation of palm fatty acid distillate over cobalt and manganese supported on activated carbon originating from waste coconut shell.

Journal of Analytical and Applied Pyrolysis 2019; **144**, 104690.

[64] H Wang, H Lin, Y Zheng, S Ng, H Brown and Y Xi. Kaolin-based catalyst as a triglyceride FCC upgrading catalyst with high deoxygenation, mild cracking, and low dehydrogenation performances. *Catalysis Today* 2019; **319**, 164-171.

[65] N Aliana-Nasharuddin, N Asikin-Mijan, G Abdulkareem-Alsultan, MI Saiman, FA Alharthi, AA Alghamdi and YH Taufiq-Yap. Production of green diesel from catalytic deoxygenation of chicken fat oil over a series binary metal oxide-supported MWCNTs. *RSC Advances* 2020; **10(2)**, 626-642.

[66] S Jovita, N Nadhifah, R Subagyo, R Tamim, EP Ramdhani, H Holilah, N Asikin-Mijan, H Bahruji, RE Nugraha, AA Jalil, S Suprapto and D Prasetyoko. Synthesis of NiO/mesoporous aluminosilicate nanoparticles using natural template for green diesel production: the effect of Si/Al ratio. *Biomass and Bioenergy* 2025; **200**, 107977.

[67] MJA Romero, A Pizzi, G Toscano, G Busca, B Bosio and E Arato. Deoxygenation of waste cooking oil and non-edible oil for the production of liquid hydrocarbon biofuels. *Waste Management* 2016; **47**, 62-68.

[68] NA Rashidi, E Mustapha, YY Theng, NAA Razak, NA Bar, KB Baharudin and D Derawi. Advanced biofuels from waste cooking oil via solventless and hydrogen-free catalytic deoxygenation over mesostructured Ni-Co/SBA-15, Ni-Fe/SBA-15, and Co-Fe/SBA-15 catalysts. *Fuel* 2022; **313**, 122695.

[69] WNAW Khalit, N Asikin-Mijan, TS Marliza, MS Gamal, MR Shamsuddin, MI Saiman and YH Taufiq-Yap. Catalytic deoxygenation of waste cooking oil utilizing nickel oxide catalysts over various supports to produce renewable diesel fuel. *Biomass and Bioenergy* 2021; **154**, 106248.

[70] N Asikin-Mijan, G AbdulKareem-Alsultan, MS Mastuli, A Salmiaton, MA Mohamed, HV Lee and YH Taufiq-Yap. Single-step catalytic deoxygenation-cracking of tung oil to bio-jet fuel over CoW/silica-alumina catalysts. *Fuel* 2022; **325**, 124917.

[71] RE Nugraha, D Prasetyoko, H Bahruji, S Suprapto, N Asikin-Mijan, TP Oetami, AA Jalil, DVN Vo and YH Taufiq-Yap. Lewis acid Ni/Al-MCM-41 catalysts for H_2-free deoxygenation of Reutealis trisperma oil to biofuels. *RSC Advances* 2021; **11(36)**, 21885-21896.

[72] H Chen, Q Wang, X Zhang and L Wang. Quantitative conversion of triglycerides to hydrocarbons over hierarchical ZSM-5 catalyst, *Applied Catalysis B: Environment* 2015; **166-167**, 327-334.

[73] A Gacem, P Sambandam, S Santhosh, T Silambarasan, P Saravanan, B Bairavi, PVL Mangesh, KK Yadav, M Khalid, HA Alqhtani, M Bin-Jumah, A Subramani, C Kavitha and P Tamizhdurai. Catalytic hydroprocessing of mixed plastic waste using Ni-Ce/ZSM-5: Performance and emission analysis of diesel blends across blending ratios. *Energy Reports* 2025; **13**, 1590-1607.

[74] Khan, KM Qureshi, ANK Lup, MFA Patah and WMAW Daud. Role of Ni-Fe/ZSM-5/SAPO-11 bifunctional catalyst on hydrodeoxygenation of palm oil and triolein for alternative jet fuel production. *Biomass and Bioenergy* 2022; **164**, 106563.

[75] G Wu, N Zhang, W Dai, N Guan and L Li. Construction of bifunctional Co/H-ZSM-5 catalysts for the hydrodeoxygenation of stearic acid to diesel-range alkanes, *ChemSusChem* 2018; **11(13)**, 2179-2188.